

JGR Solid Earth

RESEARCH ARTICLE

10.1029/2019JB018614

Special Section:

Samail ophiolite, Oman, Special Collection

Key Points:

- Reaction-driven cracking is simulated using the phase-field method for brittle failure coupled to a poroelastic model of serpentinization
- Background stresses, fluid pressure gradients, and chemical diffusion of dissolved fluid components strongly affect the extent of reaction
- Enhanced fluid and mass transport in cracks lead to growing networks that feature multiple generations of orthogonally crosscutting veins

Supporting Information:

- Supporting Information S1

Correspondence to:

O. Evans,
ore2000@columbia.edu

Citation:

Evans, O., Spiegelman, M., & Kelemen, P. B. (2020). Phase-field modeling of reaction-driven cracking: determining conditions for extensive olivine serpentinization. *Journal of Geophysical Research: Solid Earth*, 125, e2019JB018614. <https://doi.org/10.1029/2019JB018614>

Received 28 AUG 2019

Accepted 21 NOV 2019

Accepted article online 22 NOV 2019

Phase-Field Modeling of Reaction-Driven Cracking: Determining Conditions for Extensive Olivine Serpentinization

Owen Evans¹, Marc Spiegelman^{1,2,3}, and Peter B. Kelemen^{2,3}

¹Department of Applied Physics and Applied Mathematics, Columbia University, Columbia, NY, USA,

²Lamont-Doherty Earth Observatory, Columbia University, Palisades, NY, USA, ³Department of Earth and Environmental Sciences, Columbia University, NY, USA

Abstract The motion of plates leads to cycling of chemically bound water and volatiles through the Earth's interior, having consequences for arc magmatism and seismic activity at subduction zones. Tectonically exhumed peridotite at the Earth's surface provides a substantial sink for water and carbon. The natural chemical disequilibrium that exists between exposed mantle peridotite and the surface waters/atmosphere could potentially be harnessed as a negative carbon emission technology. Understanding this process is therefore critical from both a petrological and environmental perspective. Retrograde metamorphism is physically complex, potentially involving an interplay between positive (cracking) and negative (clogging) feedbacks that may limit, or promote, fluid supply to unreacted minerals. Modeling studies are important in helping to constrain the conditions that control the extent of reaction in ultramafic rocks. This study builds on a previously reported model that describes olivine hydration/carbonation in a poroelastic medium, coupling fluid flow, elastic deformation, and mass transfer between chemically active phases. Here we extend this model to include brittle failure, which is crucial given the widely held hypothesis that reaction-driven cracking is the dominant positive feedback in these processes. Here we explore the use of phase-field methods to simulate brittle failure in a poroelastic medium, in the context of hydration (serpentinization) of peridotite. We show that reaction-driven cracking in this model can generate a positive feedback that, under certain conditions, can lead to 100% transformation of olivine to serpentine.

1. Introduction

Alteration of ultramafic rocks plays an important role in a wide range of geophysical and geochemical processes, as well as supporting marine ecosystems (Martin et al., 2008; Sleep et al., 2004) and, increasingly, providing a potential sink for carbon in engineered processes for reversing anthropogenic climate change (Seifritz, 1990; Lackner et al., 1995). Hydration of the oceanic plate near spreading centers (Craft and Lowell, 2009; Roland et al., 2010) and trench outer-rise regions (Ranero et al., 2003; Van Avendonk et al., 2011) controls the volume of water that is carried into the Earth by subducting slabs, which has implications for, for example, arc magmatism (Kelley et al., 2006), intermediate-depth seismicity (Peacock, 2001), and the rheology of oceanic plate boundaries (Hirauchi et al., 2016). Carbonation of ultramafic rocks in a variety tectonic settings is thought to be a key component in the global carbon cycle (Kelemen and Manning, 2015). Mantle peridotite reacts rapidly with the atmosphere and surface waters in regions of the Earth where it is tectonically exposed at the surface. For example, analyses of peridotite outcrops in Oman indicate that present-day alteration consumes approximately 10^4 – 10^5 t of CO₂ per year (Chavagnac, Ceuleneer, et al., 2013; Chavagnac, Monnin, et al., 2013; Kelemen and Matter, 2008; Kelemen et al., 2011; Mervine et al., 2014). This has led to a renewed interest in the idea that natural olivine carbonation could be exploited as a viable carbon capture and storage method (Kelemen and Matter, 2008; Kelemen et al., 2011).

Hydration and carbonation of ultramafic rocks increase both the solid mass and volume occupied by solid phases (>50% volume increase). This process could result in clogging of pore space and armouring of surfaces by reaction products, potentially preventing the reaction from continuing. Completely carbonated (listvenites) and hydrated (serpentinites) peridotites are, however, frequently observed in outcrops,

suggesting that under certain conditions the reaction is not self-limiting. A robust observation in partially/completely altered rocks is the prevalence of dense, hierarchical crack networks extending to the grain scale. Macdonald and Fyfe (1985) proposed that solid volume changes associated with these reactions can generate stresses significant enough to fracture the rock. The generation of cracks via this process—also known as “*reaction-driven cracking*”—has been hypothesized to create a positive feedback where new fluid pathways are created and fresh reactive surfaces are exposed, offering a potential mechanism to explain the high fractions of serpentinization/carbonation observed in nature (Jamtveit et al., 2008; Iyer et al., 2008; Kelemen and Matter, 2008; Kelemen et al., 2011; Kelemen and Hirth, 2012; Macdonald and Fyfe, 1985; O’Hanley, 1992).

Reaction-driven cracking has been observed in experiments involving both carbonation of olivine (Xing et al., 2018; Zhu et al., 2016) and hydration of magnesium oxide (Zheng et al., 2018). Other experiments on analogue systems have demonstrated that hydration reactions involving lime (Lambart et al., 2018; Wolterbeek et al., 2018) and bassanite (Skarbek et al., 2018) can produce significant crystallization-induced stresses. However, the conditions under which positive feedbacks (cracking) overcome negative feedbacks (clogging) remain relatively uncertain. There have been several efforts to quantitatively analyze these processes via simple toy models (e.g., Rudge et al., 2010) and two-dimensional numerical simulations (see e.g., Malvoisin et al., 2017; Malthe-Sørensen et al., 2006; Røyne et al., 2008; Ulven, Jamtveit, et al., 2014; Ulven, Storheim, et al., 2014). Despite the success of some of these models in their ability to produce features of altered rocks that are qualitatively persuasive (notably the “mesh” texture observed in serpentinites O’Hanley, 1992), none of the models in the aforementioned studies conserve mass for the fluid phase. This is a critical omission for several reasons, not least because the assumption of a universally present fluid phase precludes the limiting behavior that would result from pore closure and permeability decrease. The fluid phase in these models is typically represented by a massless mobile phase that is transported diffusively, not accounting for any feedbacks between reaction, permeability, and fluid availability. Models that include both positive and negative feedbacks are required to explain the range of observations.

A model description of these processes should—at a minimum—conserve mass and momentum for a fluid-infiltrated, multiphase solid that includes reactions between phases and failure of the solid framework. Evans et al. (2018) presented a model of serpentinization based on small-strain poroelasticity with fluid flow and reaction. Although this model did not include failure, numerical simulations did predict that serpentinization of an abyssal peridotite could generate tensile stresses sufficient to fracture—even for relatively small porosities ($\phi \sim 1\text{--}2\%$). The total amount of reaction in these models is limited because the available fluid is exhausted to the point where the permeability is closed off, preventing additional fluid from being brought in from elsewhere. The purpose of this paper is to explore the behavior of this model when failure is included and in particular address whether this can increase the total amount of reaction. The paper is organized as follows. Section 2 introduces the method for simulating brittle failure, followed by a description of the governing equations, constitutive choices, and nondimensionalization. In section 3, we outline the experimental design of the numerical model and provide a discussion on choice of parameters used. The results of the numerical simulations are presented in section 4, followed by a discussion and conclusion in section 5.

2. Governing Equations

2.1. Brittle Failure: The Phase-Field Method

In recent years, phase-field methods have garnered significant attention as a technique for simulating fracture in brittle materials (see Ambati et al., 2015 for a comprehensive review). Within the mechanics community these methods are derived from an energy minimization-based variational reformulation of classical Griffith fracture theory (Griffith and Eng, 1921), originally suggested by Francfort and Marigo (1998) and presented in a regularized setting by Bourdin et al. (2000). This regularized formulation approximates a sharp crack discontinuity with a diffusive interface defined by an auxiliary variable. This variable—the phase field—interpolates between fully intact and fully broken states in a smooth manner. Thermodynamically consistent continuum phase-field models of brittle fracture were later proposed by Miehe, Hofacker, and Welschinger (2010), Miehe, Welschinger, and Hofacker (2010), Borden et al. (2012), (2014), and Verhoosel and de Borst (2013).

The variational formulation in Francfort and Marigo (1998) yields a minimization problem for the energy functional

$$E(\mathbf{u}, \Gamma) = \int_{\Omega} \Psi_0 \, d\mathbf{x} + \int_{\Gamma} G_c \, ds, \quad (1)$$

where $\Omega \subset \mathbb{R}^n$ represents the spatial domain, $d\mathbf{x}$ is an infinitesimal volume element, ds is an infinitesimal surface element, Ψ_0 is the elastic energy density function, \mathbf{u} is the displacement, G_c is the material fracture toughness (with units of $J m^{-2}$), and Γ is an internal discontinuity representing a set of discrete crack surfaces. In what follows we assume an isotropic linear, homogeneous, elastic solid, subject to small deformations and deformation gradients, such that the elastic energy density is defined in terms of the Cauchy strain tensor ϵ as follows:

$$\Psi_0(\epsilon) = \frac{1}{2} \lambda \epsilon_{ii} \epsilon_{jj} + G \epsilon_{ij} \epsilon_{ij}, \quad (2)$$

where λ is the first Lamé parameter and G is the elastic shear modulus. Minimization of the functional in equation (1) is problematic in the sense that a numerical discretization must account for a set of discontinuities Γ that are not known a priori. Building on the work of Ambrosio and Tortorelli (Ambrosio and Tortorelli, 1990), the regularization derived by Bourdin et al. (2000) bypasses this issue by approximating the fracture surface Γ by a phase-field $d(\mathbf{x}) \in [0, 1]$. The phase field is a dimensionless variable that represents a fully fractured state when $d = 1$ and an intact state when $d = 0$. Following Bourdin et al. (2000), a regularization of the crack functional yields

$$\int_{\Gamma} G_c \, ds \approx G_c \int_{\Omega} \gamma(d, \nabla d) \, d\mathbf{x}, \quad (3)$$

which leads to the following regularized energy functional

$$E_l(\mathbf{u}, d) = \int_{\Omega} \Psi_0 \, d\mathbf{x} + G_c \int_{\Omega} \gamma(d, \nabla d) \, d\mathbf{x}. \quad (4)$$

The crack surface density function per unit volume γ is defined as

$$\gamma(d, \nabla d) := \frac{1}{2l} d^2 + \frac{l}{2} |\nabla d|^2, \quad (5)$$

where l is a lengthscale parameter that controls the localization of d , that is, the transition width between $d = 1$ and $d = 0$ in a region representing a crack. Using the notion of Γ convergence (see Bourdin et al., 2000 for details), it can be shown that the regularized energy functional in equation (4) approximates the energy functional in equation (1) in the limit as $l \rightarrow 0$; that is, the set $\{\mathbf{x} \in \mathbb{R}^n \mid d(\mathbf{x}) = 1\}$ fully recovers the discrete crack set Γ .

A constitutive model is required to describe the loss of material stiffness due to fracture. The original form for the modified stored elastic energy $\Psi := \Psi(\epsilon, d)$ (as described in Bourdin et al., 2000) is given by

$$\Psi(\epsilon, d) = g(d) \Psi_0(\epsilon), \quad (6)$$

where $g(d)$ is an energy degradation function defined as

$$g(d) = (1 - d)^2 + \eta. \quad (7)$$

The small dimensionless parameter η acts as an artificial residual stiffness that avoids ill posedness when $d = 0$. Γ convergence for the regularized minimization problem (as $l \rightarrow 0$) has been proved for this choice of $g(d)$ (Chambolle, 2004). A critical issue with formulation (6) is that it does not differentiate between tensile and compressive failure, leading to physically unrealistic results (see Ambati et al., 2015). To address this, Amor et al. (2009) proposed a modification of (6) that leads to the definition of an anisotropic elastic energy density function:

$$\Psi(\epsilon, d) = g(d) \Psi_0^+(\epsilon) + \Psi_0^-(\epsilon), \quad (8)$$

where Ψ_0^+ and Ψ_0^- are the tensile and compressive contributions of the undamaged elastic energy density, respectively (so that $\Psi_0 = \Psi_0^+ + \Psi_0^-$). Amor et al. (2009) define Ψ_0^+ and Ψ_0^- in such a way that the degradation function g affects the tensile part of the elastic energy only—an approach known as the

“volumetric-deviatoric” split. It should be noted that Γ convergence is not guaranteed in this case. Although we choose this particular approach, alternative splits that lead to different definitions of Ψ_0^+ and Ψ_0^- have been proposed by other authors, for example, via a spectral decomposition of the strain tensor (Miehe, Hofacker, & Welschinger, 2010), and a combined cleavage-deviatoric split (Freddi and Royer-Carfagni, 2010). Following Amor et al. (2009), the tensile and compressive energy densities are defined as follows:

$$\Psi_0^+(\epsilon) = \frac{K_e}{2} \langle \text{tr}(\epsilon) \rangle_+^2 + G(\epsilon^d : \epsilon^d), \quad (9)$$

$$\Psi_0^-(\epsilon) = \frac{K_e}{2} \langle \text{tr}(\epsilon) \rangle_-^2, \quad (10)$$

where $K_e = \frac{2G}{3} + \lambda$ is the elastic bulk modulus, $\epsilon^d = \epsilon - \frac{1}{3}(\text{tr}(\epsilon))\mathbf{I}$ is the deviatoric strain tensor, and $\langle \cdot \rangle_{\pm} = (\cdot \pm |\cdot|)/2$. A corresponding modification of the effective stress leads to the following constitutive relation:

$$\sigma'(\mathbf{u}, d) := \frac{\partial \Psi(\epsilon, d)}{\partial \epsilon} = g(d)\sigma'^+ + \sigma'^-, \quad (11)$$

where $\sigma'^+ = \frac{\partial \Psi_0^+(\epsilon)}{\partial \epsilon}$ and $\sigma'^- = \frac{\partial \Psi_0^-(\epsilon)}{\partial \epsilon}$. Using the definitions in (9) and (10), we obtain that

$$\sigma'^+ = K_e \langle \text{tr}(\epsilon) \rangle_+ \mathbf{I} + 2G\epsilon^d, \quad (12)$$

$$\sigma'^- = K_e \langle \text{tr}(\epsilon) \rangle_- \mathbf{I}. \quad (13)$$

Minimization of the regularized energy functional in equation (4) with respect to the phase-field d requires that

$$\frac{G_c}{l} [d - l^2 \nabla^2 d] = 2(1-d)\Psi_0^+(\epsilon), \quad (14)$$

where it has been assumed that $g(d)$ takes the form given in equation (7), though other forms could be considered (e.g., a cubic degradation function Borden et al., 2016). To prevent crack healing in the case of decreasing Ψ_0^+ , we follow Miehe, Hofacker, and Welschinger (2010) by introducing a strain-history field \mathcal{H} , which is defined as

$$\mathcal{H}(\mathbf{x}, t) := \max_{s \in [0, t]} \Psi_0^+(\epsilon(\mathbf{u}, s)). \quad (15)$$

Replacing Ψ_0^+ with \mathcal{H} in equation (14) (see Appendix A of Miehe, Hofacker, and Welschinger (2010) for details) leads to the following modified evolution equation for the phase-field d :

$$\frac{G_c}{l} [d - l^2 \nabla^2 d] = 2(1-d)\mathcal{H}. \quad (16)$$

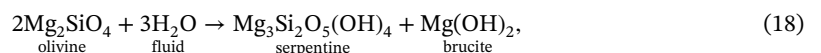
The rate-independent form in equation (16) can be modified to include a viscous regularization Miehe, Hofacker, and Welschinger (2010) as follows

$$\xi \frac{\partial d}{\partial t} = 2(1-d)\mathcal{H} - \frac{G_c}{l} [d - l^2 \nabla^2 d], \quad (17)$$

where ξ is an artificial viscosity that can help mitigate numerical stability issues.

2.2. Poroelastic-Reactive Model

Here we briefly summarize the model presented in Evans et al. (2018). This model is based on small-strain poroelasticity that includes fluid flow and reactions between phases and follows a similar derivation to equations describing magma transport in viscously deformable mantle rock (see e.g., Bercovici et al., 2001; Katz et al., 2006; McKenzie, 1984; Spiegelman et al., 2001; Rudge et al., 2011). Here we focus on the following serpentinization reaction:



where olivine combines with water to form serpentine and brucite. Following Evans et al. (2018), we make the simplifying assumption that the brucite phase can be neglected in the model, which is justified because it has a relatively small contribution to solid density changes during reaction. In particular, its exclusion does not change the sign of the total volume change due to reaction. This implies that we need only track

two immobile solid phases (olivine and serpentine) and a single mobile fluid phase (water). We also assume that the elastic moduli, compressibilities, and densities of individual phases are constant, because their variations with temperature and pressure at near-surface conditions are small relative to the bulk changes due to phase transformations on reaction. Under these assumptions, the equations for conservation of mass and momentum for the olivine-water-serpentine system undergoing this hydration reaction are as follows:

$$\nabla \cdot \sigma' - \nabla P_f + \bar{\rho} \mathbf{g} = \mathbf{0}, \quad (19)$$

$$\frac{\partial \phi}{\partial t} = (1 - \phi) \nabla \cdot \dot{\mathbf{u}} - \left[\frac{v_{ol}}{\rho_{ol}} + \frac{v_{sp}}{\rho_{sp}} \right] R, \quad (20)$$

$$\frac{\partial \phi_{sp}}{\partial t} = -\phi_{sp} \nabla \cdot \dot{\mathbf{u}} + \frac{v_{sp}}{\rho_{sp}} R, \quad (21)$$

$$\nabla \cdot \dot{\mathbf{u}} + \frac{\phi}{K_f} \frac{\partial P_f}{\partial t} = \nabla \cdot \frac{\mathbf{K}_\phi}{\mu} [\nabla P_f - \rho_f \mathbf{g}] + \left[\frac{v_f}{\rho_f} + \frac{v_{ol}}{\rho_{ol}} + \frac{v_{sp}}{\rho_{sp}} \right] R, \quad (22)$$

where ϕ is the porosity, ϕ_{sp} is the volume fraction of serpentine, P_f is the fluid pressure, \mathbf{u} is the solid displacement, and σ' is the effective stress in the solid (defined in equation (11)). ρ_i is the density of phase i (where subscript f indicates the fluid phase), v_i is related to the stoichiometric coefficients of the reaction, and R is the rate of mass transfer of the reaction (with units of $\text{kg}\cdot\text{m}^{-3}\cdot\text{s}^{-1}$). We note that the stoichiometric coefficients here represent component-wise weight percent concentrations for the reaction, which by convention are positive for products and negative for reactants (see e.g., De Groot and Mazur, 2013). The gravitational acceleration is \mathbf{g} , $\bar{\rho} = \sum_i \rho_i \phi_i$ is the phase-averaged density, K_f is the bulk modulus of the fluid, μ is the fluid viscosity, and \mathbf{K}_ϕ is the permeability tensor. The volume fraction of olivine ϕ_{ol} can be recovered from the constraint that the sum of the volume fractions must equal 1:

$$\phi + \phi_{sp} + \phi_{ol} = 1. \quad (23)$$

Equations (19)–(22) are solved in conjunction with the phase-field damage equation (17). The effective stress $\sigma' := \sigma'(\mathbf{u}, d)$ is now a function of both displacement \mathbf{u} and phase-field damage d according to its definition in equations (11)–(13).

Following Evans et al. (2018), the reaction rate can be written as

$$R = r m_{sp} \frac{A}{R_s T} S(\phi, \phi_{ol}), \quad (24)$$

where r is a kinetic rate constant ($\text{mol}\cdot\text{m}^{-2}\cdot\text{s}^{-1}$), A is the affinity of the reaction, R_s is the universal gas constant ($\text{J mol}^{-1} \text{K}^{-1}$), T is temperature (K), and m_{sp} is the molecular weight of serpentine (kg mol^{-1}). The function S represents the available surface area for reaction in terms of phase fractions. We assume that $S = a_0 \phi \phi_{ol}$, where a_0 is a reference specific surface area (per unit volume). A critical feature of the availability term S is that it goes to 0 as either one of the reactive phases (water or olivine) is exhausted, stopping the reaction altogether. In order to account for the nonelastic strain due to the reaction, we introduce an eigenstrain ϵ^* such that the true strain can be decomposed as $\epsilon = \epsilon_{el} - \epsilon^*$ (see e.g., Timoshenko and Goodier, 1970; Ulven, Jamtveit, et al., 2014), where ϵ_{el} is the standard Cauchy strain tensor. The eigenstrain ϵ^* can be written as

$$\epsilon^* = \left(\int_0^t R^*(t') dt' \right) \mathbf{I}, \quad (25)$$

where $R^*(t) := \left[\frac{v_f}{\rho_f} + \frac{v_{ol}}{\rho_{ol}} + \frac{v_{sp}}{\rho_{sp}} \right] R$.

2.2.1. Permeability

There have been various approaches to the treatment of fluid flow in cracks within the context of phase-field methods (e.g., Mikelic et al., 2015; Miehe and Mauthe, 2016; Lee et al., 2016; Santillán et al., 2017, 2018).

The majority of these approaches have been concerned with problems related to hydraulic fracturing, where fluid transport in cracks (due to injection) is rapid in comparison to the “leak-off” transfer between matrix and cracks. As Choo and Sun (2018) note, in situations where cracking is controlled by crystallization in pore space (potentially leading to clogging) and where fluid flow between the matrix and cracks is significant, it is justifiable to treat them as a continuum, rather than being governed by different equations solved on separate domains. One approach to describing the anisotropic Poiseuille flow within the cracks is to partition the absolute permeability into matrix and crack components (see e.g., Choo and Sun, 2018; Miehe and Mauthe, 2016) as follows

$$\mathbf{K}_\phi \equiv \mathbf{K}_\phi^{\text{matrix}} + \mathbf{K}_\phi^{\text{crack}}, \quad (26)$$

where $\mathbf{K}_\phi^{\text{matrix}}$ is the isotropic permeability tensor for the “uncracked” solid and $\mathbf{K}_\phi^{\text{crack}}$ is an anisotropic tensor. Following Gueguen and Dienes (1989), the uncracked permeability is parametrized in terms of the porosity as

$$\mathbf{K}_\phi^{\text{matrix}} = w_0^2 \phi^2 \mathbf{I}, \quad (27)$$

where w_0 is the characteristic microcrack width of the intact porous medium. For the cracked permeability we adopt the approach taken by Miehe and Mauthe (2016), which describes the enhanced fluid flow along cracks as

$$\mathbf{K}_\phi^{\text{crack}} = d^2 w_0^2 \phi^2 (\mathbf{I} - \mathbf{n}_d \otimes \mathbf{n}_d), \quad (28)$$

where d is the phase field and $\mathbf{n}_d = \frac{\nabla d}{|\nabla d|}$ is a unit vector orthogonal to the crack orientation. The above form is derived from the assumption that Poiseuille flow in cracks is governed by a quadratic dependence on the crack opening (Miehe and Mauthe, 2016), which in our model is parametrized in terms of the porosity. This form captures the effects of permeability changes due to fluid transfer between the bulk and cracks and clogging by precipitation of reaction products. The operator $(\mathbf{I} - \mathbf{n}_d \otimes \mathbf{n}_d)$ projects onto the line parallel to the crack orientation, resulting in maximum enhancement in the direction parallel to the crack and zero enhancement orthogonal to it. It should be noted that the functional form for the permeability—and the crack permeability especially—is a considerable source of uncertainty and should be explored in more depth (ideally in the context of experiments).

2.2.2. Scaling

Equations (17) and (19)–(22) are scaled as follows:

$$\mathbf{x} = [x]\mathbf{x}', \quad (\phi, \phi_{ol}, \phi_{sp}) = ([\phi]\phi', [\phi_{ol}]\phi'_{ol}, [\phi_{sp}]\phi'_{sp}),$$

$$(K_e, G) = [K_e](K'_e, G'), \quad t = \frac{[x]}{[v_f]} t',$$

$$K_\phi = [K_\phi]K'_\phi, \quad P_f = [P_f]P'_f,$$

$$\mathbf{u} = [u]\mathbf{u}', \quad l = [x]l',$$

where primed terms indicate dimensionless variables and bracketed terms are the characteristic scalings. The scaled mean fluid velocity $[v_f]$ can be written as

$$[v_f] = \frac{[K_\phi][P_f]}{\mu[x][\phi]}, \quad (29)$$

where the $[P_f] = [\phi][K_e]$ and $[K_\phi] = w_0^2[\phi]$. The reference displacement is $[u] = [x][\phi]$. In terms of dimensionless variables equations (17) and (19)–(22) can now be written as (dropping primes):

$$\nabla \cdot \sigma' - \nabla P_f + \frac{\mathcal{G}\bar{\rho}}{\rho_f} \hat{\mathbf{g}} = \mathbf{0}, \quad (30)$$

$$\frac{\partial \phi}{\partial t} = (1 - [\phi]\phi) \nabla \cdot \dot{\mathbf{u}} + R_\phi \phi \phi_{ol}, \quad (31)$$

$$\frac{\partial \phi_{sp}}{\partial t} = -[\phi]\phi_{sp}\nabla \cdot \dot{\mathbf{u}} + R_{\phi_{sp}}\phi\phi_{ol}, \quad (32)$$

$$\nabla \cdot \dot{\mathbf{u}} + \beta\phi\frac{\partial P_f}{\partial t} = \nabla \cdot K_\phi [\nabla P_f - G\hat{\mathbf{g}}] + R_{P_f}\phi\phi_{ol}, \quad (33)$$

$$\frac{\partial d}{\partial t} = -[d - l\nabla^2 d] + 2(1 - d). \quad (34)$$

The following dimensionless parameters emerge from these scalings:

$$\mathcal{G} = \frac{\rho_f g[x]}{[\phi][K_e]}, \quad (35)$$

$$Da = \frac{R'[x]|\nu_{ol}|[\phi_{ol}]}{[\nu_f]\rho_{ol}}, \quad (36)$$

$$\beta = \frac{[\phi][K_e]}{K_f}, \quad (37)$$

$$\mathcal{A} = \frac{G_c}{[K_e]l}, \quad (38)$$

$$\mathcal{M} = \frac{\xi[\nu_f]}{[x][K_e]}, \quad (39)$$

where \mathcal{G} is the elastogravity number, Da is the Damköhler number, β is the relative fluid compressibility, \mathcal{A} is the Griffith ratio, \mathcal{M} is the dimensionless artificial viscosity, and $R' = rm_{sp}a_0A/R_sT$. The parameters R_ϕ , $R_{\phi_{sp}}$ and R_{P_f} appearing in (31)–(33) are scalings of Da , defined as

$$R_\phi = Da \left[1 + \frac{\nu_{sp}\rho_{ol}}{\nu_{ol}\rho_{sp}} \right], \quad (40)$$

$$R_{\phi_{sp}} = -Da \frac{[\phi]}{[\phi_{sp}]} \frac{\nu_{sp}\rho_{ol}}{\nu_{ol}\rho_{sp}}, \quad (41)$$

$$R_{P_f} = -Da \left[1 + \frac{\nu_f\rho_{ol}}{\nu_{ol}\rho_f} + \frac{\nu_{sp}\rho_{ol}}{\nu_{ol}\rho_{sp}} \right]. \quad (42)$$

Section 3.2 discusses the range of geologically reasonable scale parameters for a specific problem, which are listed in Table 1.

3. Model Setup

Unless stated otherwise, all simulations presented herein are based on the same model domain and sets of initial and boundary conditions. The solid phase is assumed to represent a porous block of unreacted olivine that is saturated with a small volume of fluid. The equations were solved using the open-source software TerraFERMA (Wilson et al., 2017), which leverages the FEniCS (Alnæs et al., 2015) and PETSc (Balay et al., 2019) libraries for constructing reproducible finite element models. To solve this system of equations we adopt the operator split strategy proposed by Miehe, Hofacker, and Welschinger (2010), which has been demonstrated to be extremely robust and much faster to solve than the full monolithic formulation outlined in Miehe, Hofacker, and Welschinger (2010). This solution strategy is summarized in Algorithm 1. The supporting information provides additional details of the numerical implementation, including discretization, time stepping schemes, and links to the computational codes.

Algorithm 1 Staggered solution scheme

```

1:  $t = 0, k = 0$ 
2: Initialize  $\mathbf{u}^0, \phi^0, \phi_{sp}^0, P_f^0$  and  $d^0$ 
3: while  $t < t_{\text{end}}$  do
4:   Solve (30) - (33) for  $\mathbf{u}^{k+1}, \phi^{k+1}, \phi_{sp}^{k+1}$  and  $P_f^{k+1}$  at current time  $t$ 
5:   Compute updated strain energy density  $\Psi_0^+(\epsilon(\mathbf{u}^{k+1}))$ 
6:   Update strain history as follows:
7:   if  $\Psi_0^+(\epsilon(\mathbf{u}^{k+1})) > \mathcal{H}^k$  then
8:      $\mathcal{H}^{k+1} = \Psi_0^+(\epsilon(\mathbf{u}^{k+1}))$ 
9:   else
10:     $\mathcal{H}^{k+1} = \mathcal{H}^k$ 
11:   Solve (34) for  $d^{k+1}$ 
12:   Update  $t$ :  $t += \Delta t$ 
13:   Update  $k$ :  $k += 1$ 

```

3.1. Initial and Boundary Conditions

The model domain is a rectangle of dimensions 1 by 0.5 m. The solid phase is assumed to be pure olivine at $t = 0$, so we set the initial serpentine fraction to be $\phi_{sp}(t = 0) = 0$ everywhere. The porosity is set to be largest at the left boundary ($x = 0$) and exponentially decreasing toward the right boundary ($x = 1$), that is,

$$\phi(t = 0) = \phi_{\max} \exp[-(x/x_\lambda)^2] + \phi_e, \quad (43)$$

where ϕ_{\max} is the maximum value, ϕ_e is a background value, and x_λ controls the width of the exponential tail. A smooth transition from high porosity at the boundary to low porosity in the interior is preferred as abrupt changes are more difficult to resolve numerically once cracks open up. We initially assume that this model

Table 1
Table of Parameters: Definitions (Units), Symbols, and Values

System size (m)	[x]	1
Reference porosity	$[\phi]$	0.1
Reference olivine fraction	$[\phi_{ol}]$	1
Reference serpentine fraction	$[\phi_{sp}]$	1
Characteristic microcrack width (m)	w_0	$10^{-8}\text{--}10^{-6}$
Reference permeability (m^2)	$[K_\phi]$	$10^{-17}\text{--}10^{-13}$
Initial fracture porosity (%)	ϕ_0	1–5
Scaled affinity	$A/R_s T$	16
Kinetic rate constant ($\text{mol}\cdot\text{m}^{-2}\cdot\text{s}^{-1}$)	r	$10^{-12}\text{--}10^{-8}$
Viscosity of water (Pa s)	μ	8.90×10^{-4}
Reference bulk modulus (Pa)	$[K_e]$	10^{11}
Dimensionless bulk modulus	K_e	0.01–1
Dimensionless shear modulus	G	0.005–0.5
Relative compressibility	β	5–500
Damköhler number	Da	$10^{-6}\text{--}10^2$
Griffith ratio	\mathcal{A}	$10^{-8}\text{--}10^{-5}$
Artificial viscosity (Pa s)	ξ	10^{-6}
Residual stiffness	η	10^{-5}
Density of olivine (kg m^{-3})	ρ_A	3,300
Density of serpentine (kg m^{-3})	ρ_B	2,537
Density of water (kg m^{-3})	ρ_f	1,000
Molecular weight of 2 mol of olivine (kg mol^{-1})	m_{ol}	0.281
Molecular weight of serpentine + brucite (kg mol^{-1})	m_{sp}	0.335
Molecular weight of 3 mol of water (kg mol^{-1})	m_f	0.055

describes serpentinization in a seafloor setting, where porosities of 1–5% are reasonable. This serves as a reference problem to explore the extent of serpentinization driven by spontaneous infiltration in the absence of an external fluid flux or solid stress state. We will later relax these assumptions to explore such effects. The fluid pressure is set to be constant on all boundaries and initially set to be $P_f(t = 0) = 10$ MPa everywhere (i.e., the hydrostatic pressure at a seafloor depth of 1,000 m). The normal and tangential components of the effective stress normal to the left and right boundaries are set to be 0. The displacements normal to the top and bottom boundaries are set to be 0, except in the case of section 4.3, where we apply a small normal stress at these boundaries. The phase field is initially 0 everywhere and satisfies $\nabla d \cdot \mathbf{n} = 0$ on all boundaries.

3.2. Parameters

When the degradation function takes the form $g(d) = (1 - d)^2$, the tensile strength σ_T can be expressed as (Amor et al., 2009; Borden et al., 2012)

$$\sigma_T = \frac{9}{16} \sqrt{\frac{EG_c}{3l}}, \quad (44)$$

where E is the Young's modulus. A value for the ratio G_c/l can be estimated from known tensile strengths and elastic moduli for a particular material. The tensile strength of peridotite is estimated to be somewhere in the range of 5–20 MPa (Cai, 2010). Measured elastic moduli (at zero confining pressure) for olivine are $[K_e] = 129.4$ GPa and $[G] = 78$ GPa (Abramson et al., 1997). These values are considered upper bounds on the true elastic moduli for a fluid-saturated rock and, furthermore, will be significant overestimates for a partially serpentinized peridotite owing to the relative weakness of serpentine (Escartin et al., 2001). Assuming up to a 2 order of magnitude reduction in the elastic moduli, we estimate that $G_c/l \sim 10^3 - 10^6$. Fixing the reference elastic modulus scaling to be $[K_e] = 100$ GPa, then implies that $\mathcal{A} \sim 10^{-8} - 10^{-5}$.

Taking the reference lengthscale to be $[x] = 1$ m yields an elastogravity number of $\mathcal{G} \sim 10^{-6}$, which is small enough to justify neglecting gravitational effects in what follows. Following Evans et al. (2018), we assume microcrack widths of $w_0 \sim 10^{-8} - 10^{-6}$ m, based on estimates of crack densities (Hadley, 1976) and aspect ratios (Bonnet et al., 2001; Vermilye and Scholz, 1995) relevant to porosities in the range of $\phi \sim 1\text{--}5\%$. From this we extract reference permeabilities in the range of $[K_\phi] \sim 10^{-17}\text{--}10^{-13}$ m², which corresponds to actual permeabilities of $K_\phi \sim 10^{-15}\text{--}10^{-11}$ m² when 1% porosity is assumed. This range is consistent with observed permeabilities in tectonically exhumed mantle peridotites (e.g., Manning and Ingebritsen, 1999; Wu et al., 2006; Dewandel et al., 2005). Assuming a fluid bulk modulus of $K_f = 2.2 \times 10^9$ Pa and a reference porosity of $[\phi] = 0.1$ yields a dimensionless compressibility of $\beta \sim 5$. We note, however, that when the fluid contains a very small fraction of isolated air bubbles (termed the “insular air saturation” in the groundwater literature (Bear and Cheng, 2010)), then it is still valid to treat the fluid as a single phase, but with a mixture dependent compressibility determined by Wood's equation (see Cheng, 2016).

At near-surface conditions the change in the Gibbs free energy (at constant T and P) for the reaction in equation (18) is

$$\Delta_r G = -R_s T \ln \Omega, \quad (45)$$

where Ω is the ratio of the product of stoichiometric activities and the equilibrium reaction coefficient. The affinity for the reaction (introduced in equation (24)) is given by $A = -\Delta_r G$. For pure water in the presence of olivine at near-surface conditions it is observed that $\Omega \sim 10^7$ (Kelemen and Hirth, 2012), which implies a scaled affinity of $\frac{A}{R_s T} \sim \ln 10^7$. Experimentally determined kinetic rates for serpentinization are highly variable and temperature dependent (see Lamadrid et al. (2017) and McCollom et al. (2016) for a more detailed discussion). Following Evans et al. (2018), we consider rates in the range of $r \sim 10^{-12} - 10^{-8}$ mol m⁻² s⁻¹. All parameter values are summarized in Table 1.

4. Results

Here we present results from numerical simulations of the model outlined in the previous sections. To highlight the effects of reaction-driven cracking, we first discuss results from simulations where failure is not included. We then add failure and discuss its effect. Though this second model demonstrates feedbacks associated with reaction-driven cracking, it is somewhat idealized in that we do not consider environmental factors and/or additional processes that may be critical in determining the extent of reaction in natural systems. To illustrate some of these potential effects, we conclude this section by presenting a set of simulations

that consider, separately, scenarios that include (1) preexisting stresses within the rock, (2) fluid pumping due to a background pressure gradient, and (3) fluid transport into cracks/voids via chemical potential gradients.

4.1. No Failure

In the absence of failure we solve equations (30)-(33) only. As is discussed in Evans et al. (2018), the serpentinization reaction causes the net volume of a closed water-olivine system to decrease. This is a consequence of the relative densities of the reactants and products in that serpentine is closer in density to olivine than it is to water. Alternatively, in an open system with uninterrupted water supply and minor changes in porosity, serpentinization causes the net volume to increase. Differential volume changes within the solid give rise to tensile stresses that can eventually lead to failure in tension. This is consistent with reaction-driven cracking observed in olivine carbonation (Zhu et al., 2016; Xing et al., 2018) and periclase hydration experiments (Zheng et al., 2018), where the observed failure is attributed to mismatches in volume changes.

The model setup described in section 3 is similar to a well studied problem based on experiments where a slab of material is instantaneously cooled at its boundaries, resulting in a thermal shock and the emergence of cracks that propagate into the interior (Bahr et al., 1988; Jiang et al., 2012). The mechanism of failure in these experiments is similar to other cooling and drying problems that are associated with cracking in, for example, mud, pottery/ceramics, and columnar jointing (Goehring et al., 2009), where relative differential shrinkage within the solid generates stresses. Modeling the thermal cracking problem is a significant computational challenge that has been successfully demonstrated using both gradient damage (Bourdin et al., 2014) and phase-field damage methods (Farrell and Maurini, 2017). The problem described in this paper is further complicated by the fact that this is a fluid-saturated poroelastic medium rather than a purely elastic solid.

The simulation shown in Figure 1 has been run until all the initial fluid has been consumed by the reaction and the solid framework has become impermeable, at which point there is no fluid transport from the boundaries into the domain. Cessation of the reaction (due to a lack of reactive fluid) is a departure from previous models (e.g., Røyne et al., 2008; Ulven, Jamtveit, et al., 2014), that, by construction, permit constant replenishment of the mobile phase via diffusion from the boundaries, neglecting any negative feedbacks introduced by the reaction (i.e., pore closure and permeability reduction). Figure 1a shows the initial porosity field, which is ~4.5% at the left boundary and decreases exponentially toward the right boundary where there is a small residual background porosity of ~0.5%. Figures 1b and 1c show the state of the system at the final run time. The reaction of water and olivine produces serpentine in the region in the vicinity of the left boundary (see panel b). Once completely reacted with the olivine, at the left boundary (where the initial porosity is greatest) the degree of serpentinization is ~10%.

The negative volume change of the reaction causes a reduction in fluid pressure. As the pressure is fixed at the left boundary, this results in a pressure reduction in the interior, which drives an additional fluid flux from the left boundary. For this set of initial/boundary conditions, however, the flux is small and does not significantly increase the amount of reaction. This suggests that different conditions that lead to more significant fluid input are required to overcome rapid fluid consumption and permeability reduction. More substantial fluid fluxes (leading to more reaction) are possible if there is an initial pressure gradient across the domain or an imposed flux at the left boundary. In the case where the rock is fractured, small pressure gradients do have a significant effect on the reaction (this is discussed later in section 4.4). However, in the unfractured case where fluid flow is purely Darcian, we find that for initial porosities of <5% and pressures below the hydraulic fracturing threshold, the effect of pressure gradients/imposed fluxes on the total amount of reaction is negligible. To achieve degrees of serpentinization >15%, we would expect significant influx of fluid that is unlikely to result from purely Darcian flow through an intact permeable matrix. For example, to produce a rock that is 100% serpentinized, this system would have required a tenfold increase in the total fluid mass flux over the time taken to completely react it.

The robust observation that natural samples of highly serpentinized/carbonated peridotite are pervasively fractured down to the subgrain-scale supports the notion that Darcian flow alone is insufficient to supply large volumes of fluid, and suggests that flow along fractures may be the dominant mode of fluid transport in these rocks after the onset of failure. The results in Figure 1c show that the reaction-driven volume changes generate tensile stresses in the solid that exceed its tensile strength (in this case ~45 MPa). The most tensile principal stress (plotted in panel c) predicts that Mode I cracks would initiate at the boundary and would propagate horizontally into the domain (from left to right). We note that the conclusions drawn from these

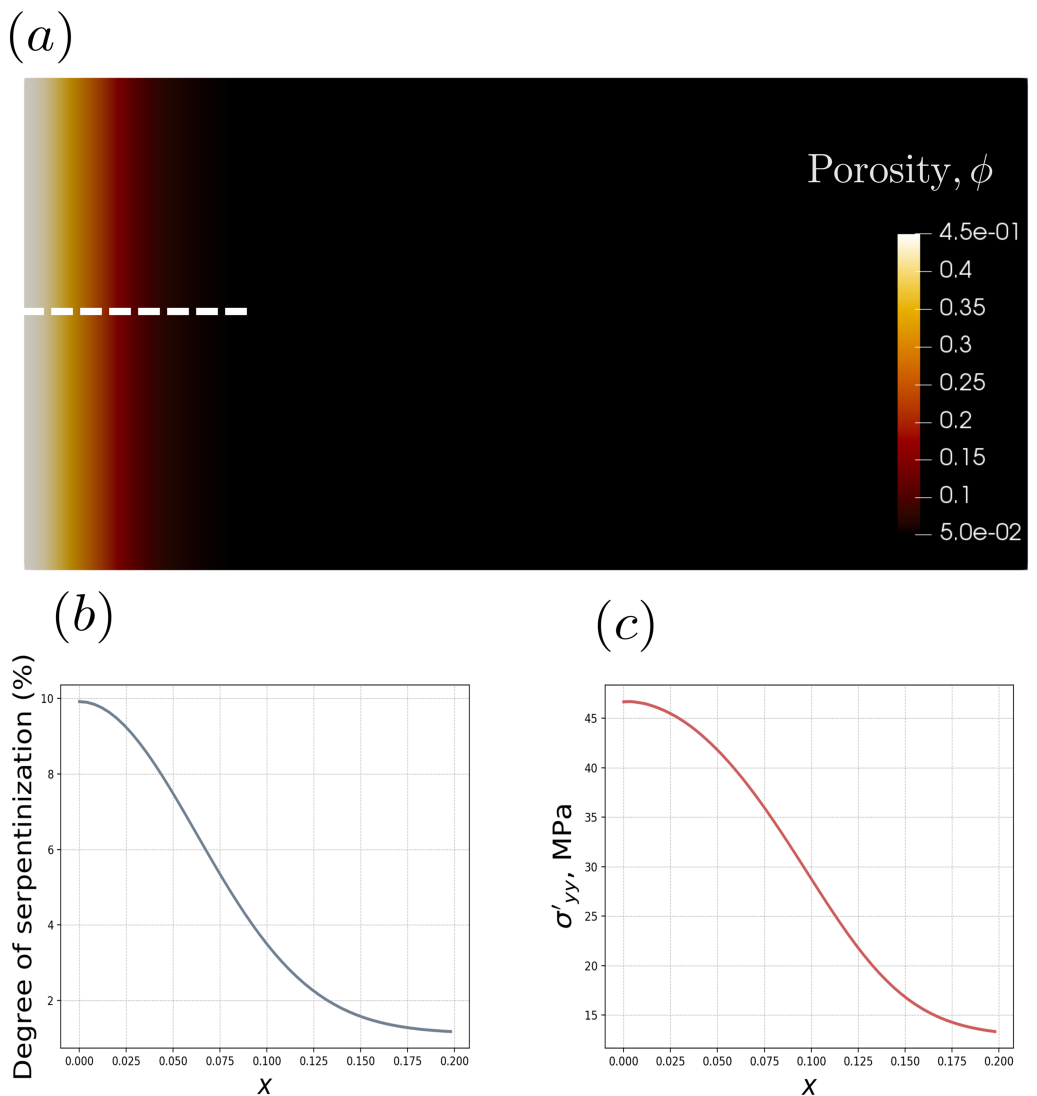


Figure 1. Panel (a) shows the porosity at $t = 0$, which is greatest at the left boundary ($\sim 4.5\%$) and tails off to a background value of 0.5% . Note that the porosity shown here is the scaled porosity, meaning that the maximum of 0.45 on the scale bar corresponds to a true porosity of 4.5% . The solutions in (b) and (c) are plotted along the white dotted line shown in (a) (going from $x = 0$ to $x = 0.2$). Plotted in panel (b) is the total amount of serpentine produced by the reaction once all available fluid has been exhausted (i.e., $\phi \approx 0$). The degree of serpentinization is greatest at the left boundary ($\sim 10\%$). Panel (c) shows the most tensile principal stress at the same time, which here coincides with σ_{yy}' . Again, this is greatest at the left boundary, corresponding to where the most reaction has taken place. The maximum value (>45 MPa) exceeds the upper bound tensile strength of peridotite by 125% , so it is expected that horizontally oriented mode I cracks will open up in this stress field. We note that both σ_{yy}' and the degree of serpentinization are uniform in the y direction.

simulations are the same as those discussed in Evans et al. (2018), which predicted stresses leading to Mode I cracking in a partially serpentinized peridotite.

4.2. Adding Failure

The results in Figures 2 and 3 show the behavior of the model that includes failure. The model is otherwise identical to that discussed in the previous section. We have assumed the rock's tensile strength to be $\sigma_T = 20$ MPa. Failure is expected here as we have already demonstrated that this set of parameters and initial/boundary conditions will lead to tensile stresses that exceed this limit (see Figure 1c). The length-scale parameter l that appears in equation (34) controls the width of the damage zone; here we take this to be $l = 0.01$. The residual stiffness η and viscous regularization ξ parameters that were introduced in equations (7) and (17), respectively, are chosen to be $\eta = 10^{-5}$ and $\xi = 10^{-6}$. Miehe, Hofacker, and

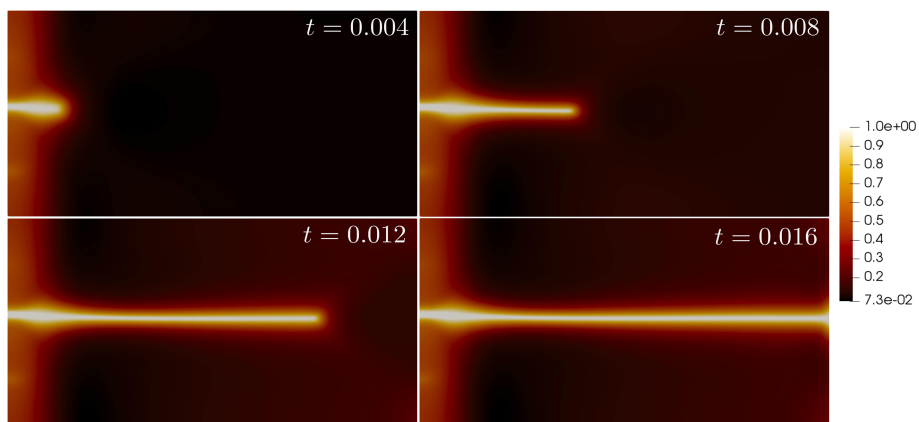


Figure 2. Evolution of the phase-field d at uniformly spaced times between $t = 0.004$ and $t = 0.016$. Bright and dark colors represent fully broken ($d = 1$) and intact ($d = 0$) states, respectively. Tensile stresses driven by contraction in the reactive zone near the left boundary lead to horizontally oriented Mode I failure, consistent with the stress field shown in Figure 1c. The single crack that opens up at the left boundary gradually migrates toward the right boundary. The background porosity (~0.5%) is alone insufficient to generate enough reactive stress to fracture; however, stress concentrations at the crack tip allow it penetrate this region until it hits the right boundary.

Welschinger (2010) note that the mesh size h should satisfy

$$h < \frac{l}{2}, \quad (46)$$

in order to resolve the regularized crack surface. The mesh size in this example is $h \approx 0.001$ (a mesh consisting of $\sim 10^6$ elements) so to ensure that the discretization is sufficiently resolved.

The results in Figure 2 show the emergence of a single Mode I crack at the left boundary, which gradually migrates toward the right boundary until it completely perforates the domain. The reaction-generated stresses first exceed the tensile strength at the left boundary because the initial porosity is greatest there. The crack opening leads to a positive volumetric strain (see Figure 3b) and a drop in fluid pressure around the crack tip (Figure 3c). Mass conservation requires that local solid divergence is accompanied by an increase in fluid mass. Fluid is transported into the void space generated by cracking as a response to the negative pressure gradient that develops between the crack tip and the boundary. Moreover, fluid flow along the length of the crack is enhanced by the increase in permeability as $d \rightarrow 1$ (see equation (28)). The fluid fraction increases in the crack as more fluid mass is added (Figure 3a), which leads to more reaction there relative to the bulk (Figure 3d). A comparison between the final reaction product in the models with and without failure shows that the degree of serpentinization is higher when cracking is included (a maximum of 13% vs. 10%). Moreover, the extent of reaction is now ~ 10 times greater in the damaged region than in the unfractured bulk, though it should be noted that this ratio will depend on the maximum value of initial porosity relative to the background value (the latter being $\sim 0.5\%$ here). Overall, these results support the notion that reaction-driven cracking can provide a positive feedback; that is, cracks create space for additional fluid (rapidly transported from boundaries/external fluid sources) to increase the total amount of reaction.

A notable feature of the results shown in Figures 2 and 3 is that the crack propagates into the low-permeability region ahead of the initial condition. That the model demonstrates this behavior is important because the supply of fluids to dry regions is critical for large-scale hydration/carbonation in low-permeability rocks. Surface energy-driven imbibition (Evans et al., 2018) and/or transport in nanopores (Plümper et al., 2017) may also be responsible for fluid infiltration at finer scales; for example, in transporting fluids from cracks into low-permeability rock matrix. In these simulations, crack propagation is driven by reaction in the zone around the crack tip. In the absence of reaction, stress concentrations at the tip alone are insufficient to extend the crack beyond the initial porosity layer at the left boundary. Rapid fluid transport from the left boundary to the tip is therefore crucial for the crack to propagate here. Figures 3e and 3f show the vertical ($\sigma_{yy'}$) and horizontal ($\sigma_{xx'}$) normal stress components respectively, indicating that dominant vertical tension at the tip will drive horizontal crack propagation toward the right boundary. We note that the extent of crack propagation depends also on the boundary conditions. In this case, the free boundary at $x = 1$ allows the crack to extend all the way to the right boundary; however, this would be would

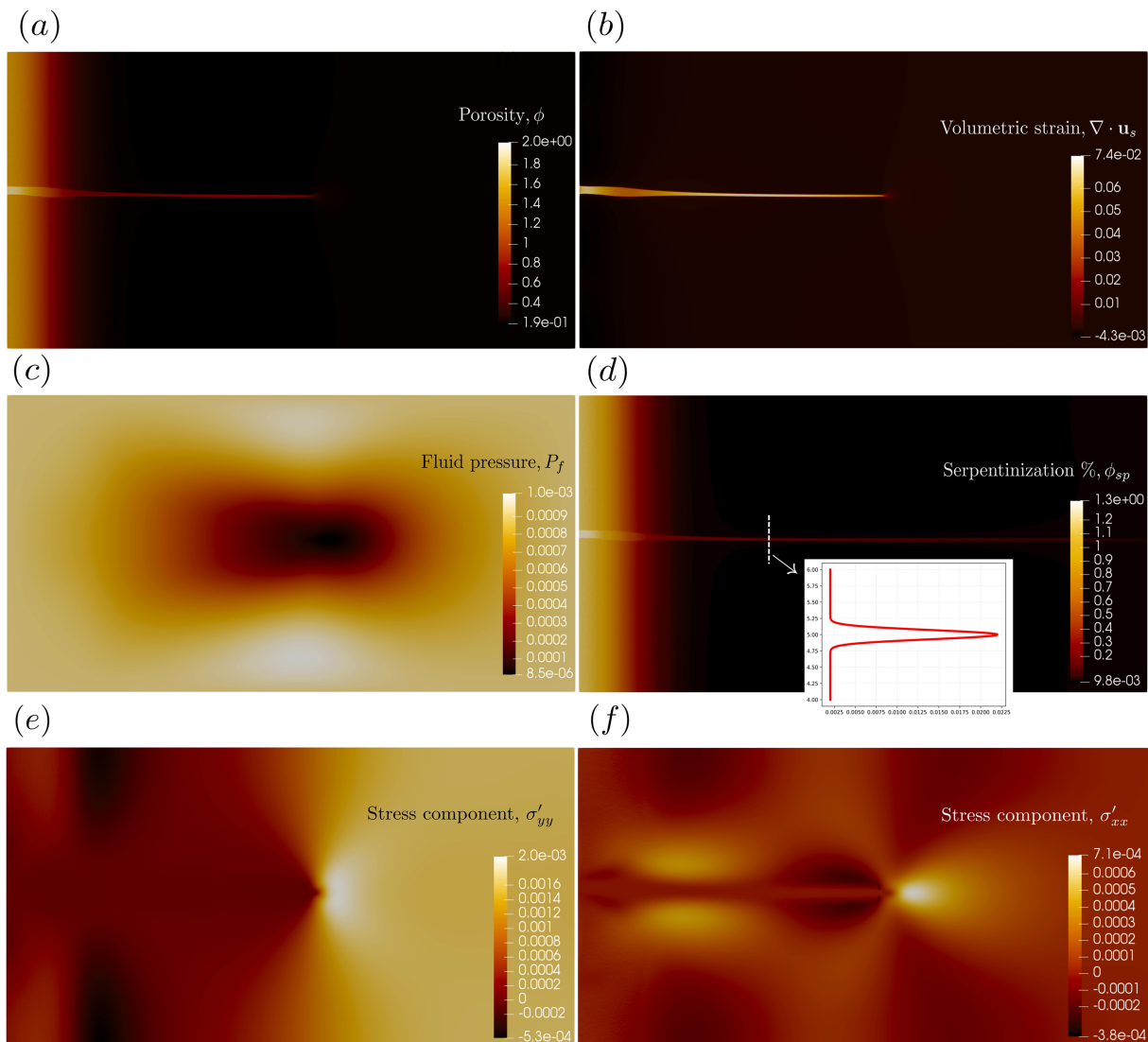


Figure 3. Damage feedbacks: solutions at $t = 0.01$ for the (a) porosity ϕ , (b) volumetric strain $\nabla \cdot \mathbf{u}$, and (c) fluid pressure P_f . The final degree of serpentinization is shown in panel (d). The crack opening leads to volume expansion, that is, positive $\nabla \cdot \mathbf{u}$ (see panel b). The fluid pressure in the crack drops (see panel c), which drives fluid flow from the left boundary toward the crack tip via the connected permeability pathway. The rate of fluid flow is enhanced in the crack due to the anisotropic component of the permeability tensor (see equation (26)). Panel (d) shows that the maximum final degree of reaction is higher in this model versus the previous one (13% vs. 10%). The red curve in the small subfigure here shows the degree of serpentinization plotted vertically along the white dotted line, which indicates a sharp increase of serpentinization in the crack. Panels (e) and (f) show the vertical σ_{yy}' and horizontal σ_{xx}' components of the normal effective stress, respectively. The most tensile stresses are concentrated at the crack tip, where the maximum tensile stress of ~ 20 MPa coincides with σ_{yy}' . This stress field leads to continued horizontal crack propagation.

be limited if, for example, we were to prescribe a zero normal displacement condition at $x = 1$. Moreover, further crack growth may also be limited if there is sufficient stress relaxation due to an accumulation of multiple cracks (see section 4.5).

As an aside we note that, although these results show the initiation and growth of a single crack, it is possible to increase the number of cracks by making the porosity gradient steeper near the boundary. The reasoning behind this is analogous to crack formation in the thermal shock problem, where semianalytical (Sicsic et al., 2014) and numerical (Bourdin et al., 2014) studies have shown that the periodicity of crack nucleation depends on the initial temperature jump at the boundary. We choose the gradient here to be mild enough that only a single crack forms. This demonstrates the basic behavior of the system and is advantageous from a numerical standpoint because the elastic subproblem becomes more ill conditioned as the number of cracks goes up. Appropriate nonlinear solvers and preconditioners have been shown to be effective at

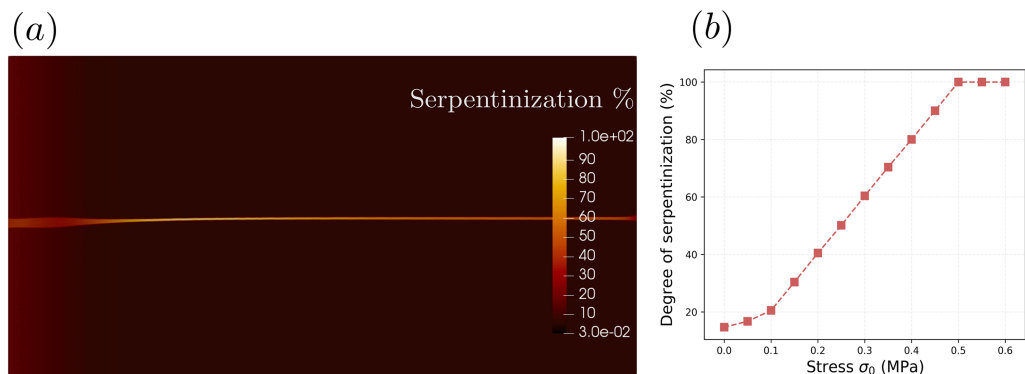


Figure 4. Reaction-driven cracking with a background stress field: (a) the degree of serpentinization (at $t = 0.05$) with a tensile stress of $\sigma_0 = 0.5$ MPa applied normal to the top and bottom boundaries and (b) plotted as a function of the applied stress σ_0 . Panel (a) shows that the rock is 100% serpentine in the crack as a result of this stress field. The vertically oriented tensile stress causes significant volume expansion in the weak zone around crack, which in turn gets filled with fluid, allowing the reaction to consume higher volumes of water. Panel (b) shows that anything exceeding 0.5 MPa leads to 100% serpentinization in the crack and the amount of reaction scales nearly linearly with the applied stress below this threshold. When $\sigma_0 = 0$, the amount of reaction is the same as that shown in Figure 3d.

dealing with this issue (Farrell and Maurini, 2017) but are beyond the scope of this work. To benchmark our implementation of the phase-field method, we have provided a comparison between our results for the thermal shock problem and the results in Farrell and Maurini (2017) (see the supporting information).

4.3. Failure in a Prestressed Environment

Tectonic and thermal stresses may also play a role in alteration processes, for example, in the development of microcracks formed in fresh peridotites that serve as initial fluid pathways for reactive fluids (Rouméjon and Cannat, 2014). Recent experiments that observed complete reaction of periclase to brucite (Zheng et al., 2018)—involving large volume changes ($>100\%$) and cracking—were performed under an applied differential stress field, which also suggests the importance of background stresses for significant alteration to take place. Here we test the effect of a preexisting stress field by applying normal stress at the top and bottom boundaries, so that the solid is initially in tension. We apply a weak tensional stress (between 0 and 0.6 MPa) in the y direction, which is around an order of magnitude smaller than the tensile strength. The initial stress field causes the solid to crack earlier (as less reactive stress is required to reach the failure threshold); however, we are interested primarily in the effect that this stress field has on the overall volume change when failure occurs.

The final degree of serpentinization in Figure 4a shows that an applied differential stress of 0.5 MPa (vertical tension) leads to 100% serpentinization in the crack. The applied stress results in significant mechanical deformation in the compliant region where $d \sim 1$, pulling on the crack from the top and bottom walls and causing it to widen in the y direction. Pressure gradients between the crack tip and left boundary drive additional fluid infiltration as the crack widens, which in turn leads to more reaction. In Figure 4b the maximum final degree of serpentinization is plotted as a function of the normal stress σ_0 . These results indicate that at a time of $t = 0.05$, the maximum extent of serpentinization—in a narrow region within and around the crack—reaches 100% when the differential stress is 0.5 MPa. At $t = 0.05$, the maximum extent of serpentinization at lower differential stresses is approximately linearly dependent on the stress.

4.4. Failure With a Background Pressure Gradient

The baseline model of failure in section 4.2 only allows for fluid flow driven by pressure gradients that are a result of the reaction or fracture opening. The volume of fluid that is added to the system could be increased if background pressure gradients are present. As was discussed in section 4.1, this is critical because highly serpentinized rocks require the input of large fluid volumes over the lifespan of the reaction. At near-surface conditions where reaction rates are fast, significant fluid pressure gradients might be necessary to overcome the rapid clogging of pore space/fractures that would prevent fluids from infiltrating unreacted regions of rock ahead of the reaction front. Here we consider the effect of a small horizontal fluid pressure gradient across the domain to simulate either a topographically or pumping-driven flow. Although the effect of a pressure gradient would likely be negligible in an unfractured rock—where fluid flows through

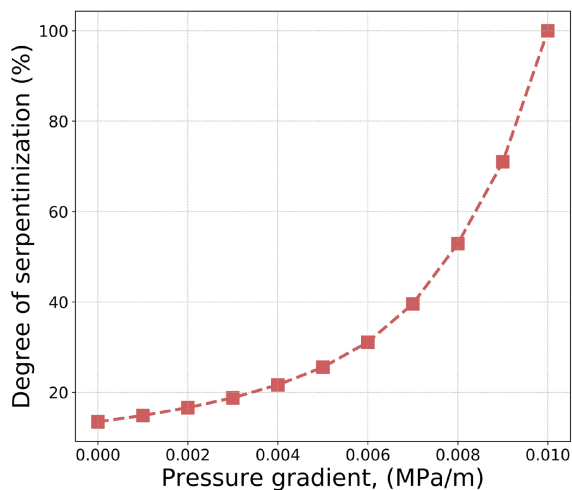


Figure 5. Reaction-driven cracking with a background fluid pressure gradient: the maximum degree of serpentinization (at $t = 0.05$) is plotted as a function of the background pressure gradient. Similar to Figure 4, the final state of the model is a highly serpentinized horizontal crack that has perforated the domain. The maximum degree of serpentinization is located within the crack. In the absence of any pressure gradient the maximum reaction is identical to that in Figure 3d. The amount of reaction increases nonlinearly with the size of the pressure gradient. The horizontal crack is 100% serpentinized once the gradient exceeds 10^{-2} MPa/m.

a low permeability network of microcracks—it could be significant when high permeability macrocracks are present.

Here we apply a negative pressure gradient in the x direction such that the pressure is largest at the left boundary and zero at the right boundary. We find that this pressure gradient has a notable effect on the amount of reaction when its value at the left boundary exceeds $\sim 10^{-3}$ MPa/m. We note, however, that this threshold will be depend on the Damköhler number. This is because higher reaction rates (i.e., larger Da) will consume fluid at a faster rate, meaning that a larger pressure gradient is required to flux the same volume of fluid through the domain before the fractures become clogged with reaction products. The final state of the system (at $t = 0.05$) in these simulations is qualitatively similar to the model with an applied stress field (discussed in section 4.3 and shown in Figure 4); that is, a single horizontal crack has completely perforated the domain and undergone significant reaction. Figure 5 shows the final degree of serpentinization (at $t = 0.05$) in the crack as a function of the pressure gradient. These results show that the degree of serpentinization increases as a function of the pressure gradient, and by 10^{-2} MPa/m (representing a hydrostatic pressure gradient) has resulted in 100% serpentinization in the crack. When there is no applied gradient, the total reaction is the same as shown in Figure 3d ($\sim 13\%$). These results support the notion that pressure gradients may play an important role in replenishing fluids in reactively fractured systems.

4.5. Failure With Chemical Potential Gradient Diffusion

Up until this point we have considered the fluid phase to be pure water. However, in reality the fluid phase will consist of water plus dissolved chemical components, for example, magnesium, that can be transported

diffusively within the fluid itself. The role of non-Darcian flow may have a significant effect on the large-scale fluid and mass transport in low permeability systems. For example, Plümper et al. (2017) showed that transport in reaction-induced nanopores can be driven solely by gradients in ion concentration. To consider mass transport of this type, we can allow for the existence of multiple components within a given phase, where a general statement of mass conservation for a component k in phase i states that

$$\frac{\partial}{\partial t} \rho_i \phi_i c_i^k + \nabla \cdot \rho_i \phi_i c_i^k \mathbf{v}_i = -\nabla \cdot \mathbf{J}_i^k + v_i^k R, \quad (47)$$

where c_i^k is the concentration of component k in phase i , v_i^k is the mass-weighted stoichiometric coefficient of the reaction for that component, and \mathbf{J}_i^k is the nonadvection flux of component k within phase i . If we assume that the fluid is dominantly water plus a very small amount of magnesium concentrated at grain boundaries, then to leading order the conservation of fluid mass equation can be written as

$$\frac{\partial}{\partial t} \rho_f \phi + \nabla \cdot \rho_f \phi \mathbf{v}_f = -\nabla \cdot \mathbf{J}_f^{H_2O} + v_f R. \quad (48)$$

We assume that the nonadvection flux takes the following form:

$$\mathbf{J}_f^{H_2O} = -D_\phi d^n \nabla \phi, \quad (49)$$

where D_ϕ is a constant diffusion coefficient and d^n is the phase field raised to some power n . This permits fluid flow driven by gradients in chemical potentials in cracks (i.e., where $d \approx 1$). Including this term in the porosity evolution equation provides an additional mechanism to bring in fluid and thereby continue the reaction further. We note that the form in equation (49) is more restricted than similar diffusion terms used in previous models (e.g., Rudge et al., 2010; Ulven, Jamtveit, et al., 2014) in the sense that this model does not permit diffusion into undamaged areas. A typical feature of previous models is to allow diffusion of reactants into undamaged materials (with faster diffusion in damaged areas), which always drives cracking.

Effective water-in-water diffusivities for flow in cracked rocks have been estimated to be $\sim 2 \times 10^{-9}$ m 2 s $^{-1}$ (Wu et al., 2006; Wu et al., 2010; Rudge et al., 2010). We use this to obtain a value of $D_\phi = 1 \times 10^{-6}$ kg m $^{-1}$ s $^{-1}$

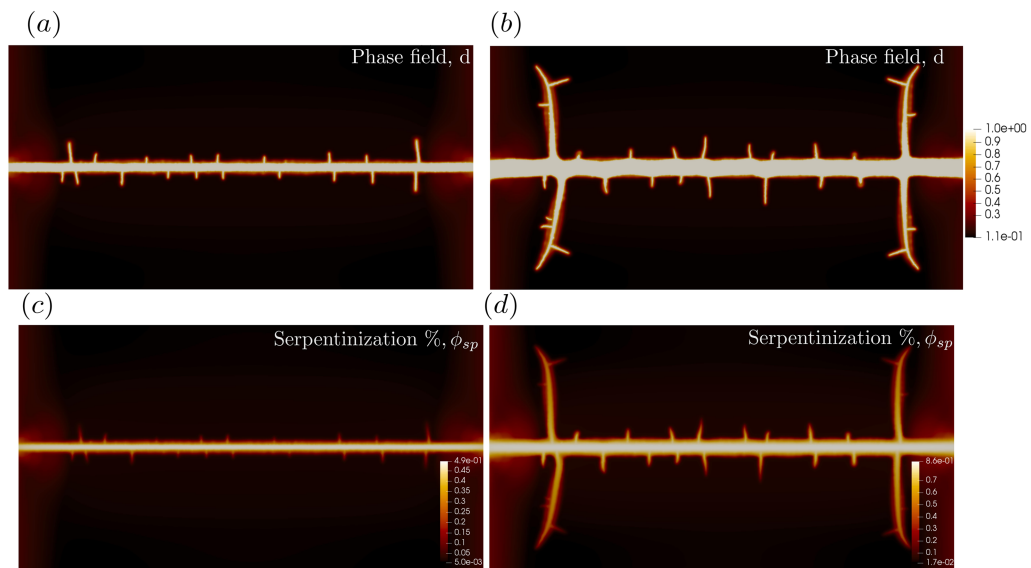


Figure 6. Cracking with enhanced water diffusion: damage and reaction progress at $t = 0.02$ (a and c) and $t = 0.04$ (b and d). These simulations include the nonadvective water flux term $\mathbf{J}_f^{H_2O} = -D_\phi d^n \nabla \phi$, where in this case $D_\phi = 1 \times 10^{-6} \text{ kg} \cdot \text{m}^{-1} \cdot \text{s}^{-1}$ and $n = 1$. Increased reaction-driven stresses lead to a second generation of cracks forming orthogonally to the first, eventually leading to an array of normally aligned cracks all the way along it (i.e., “Frankenstein” cracks). The secondary cracks migrate toward the top/bottom boundaries, and in some cases generate another set of orthogonal cracks. The fraction of serpentinization within the cracks is substantially higher than before, going from 49% at $t = 0.02$ to 86% at $t = 0.04$.

(here representing the diffusivity multiplied by the fluid density ρ_f), which appears in equation (49). For simplicity we assume that the diffusive flux depends linearly on the amount of damage, so that we may take $n = 1$ in equation (49). Figure 6 shows results that include the nonadvective flux term $\mathbf{J}_f^{H_2O}$, with $D_\phi = 1 \times 10^{-6} \text{ kg} \cdot \text{m}^{-1} \cdot \text{s}^{-1}$ and $n = 1$. We note that the boundary/initial conditions used in this section are identical to those used in sections 4.1 and 4.2 (i.e., Figures 1–3). In particular, these results do not include an applied stress field or fluid pressure gradient and should be considered distinct from the results described previously in sections 4.3 and 4.4.

Similar to the results in Figure 2, a single crack perforates the domain as it propagates horizontally from the left boundary. Diffusive fluid transport outward from this initial crack generates a thin boundary layer of fluid that extends beyond the crack walls. When D_ϕ is sufficiently large (leading to a sufficiently wide boundary layer), the reaction of fluid in this region can generate enough stress to open a second set of cracks. The anisotropic stress field resulting from the first crack will be relieved by further cracks aligned normal to it, hence producing the orthogonal system of cracks shown in Figures 6a and 6b. These are qualitatively similar to so-called “Frankenstein” crack textures that are frequently observed in outcrops of partially altered peridotite in Oman (see Figure 7 for examples). These types of textures are characterized by a central crack, flanked by a sequence of orthogonal cracks that terminate over some length scale. The results in Figure 6 show that the secondary cracks migrate toward the top/bottom boundaries and eventually form a tertiary set of orthogonal cracks. This pattern of behavior continues, while there is sufficient stress in the rock and a supply of fluid into boundary layers around the cracks; however, as is the case here, stresses within the rock are eventually relieved to the point where the cracks no longer propagate and no new ones form. In this example, diffusion coefficients that are below an order of magnitude smaller than 10^{-6} do not generate secondary sets of cracks, because boundary layer porosities in this case are insufficient to generate enough reactive stress. The extent of reaction observed within the cracks here is considerably higher than in the original failure model discussed in section 4.2: by $t = 0.02$ the degree of serpentinization is $\sim 49\%$ (Figure 6a), and by $t = 0.04$ it is $\sim 86\%$ (Figure 6c).

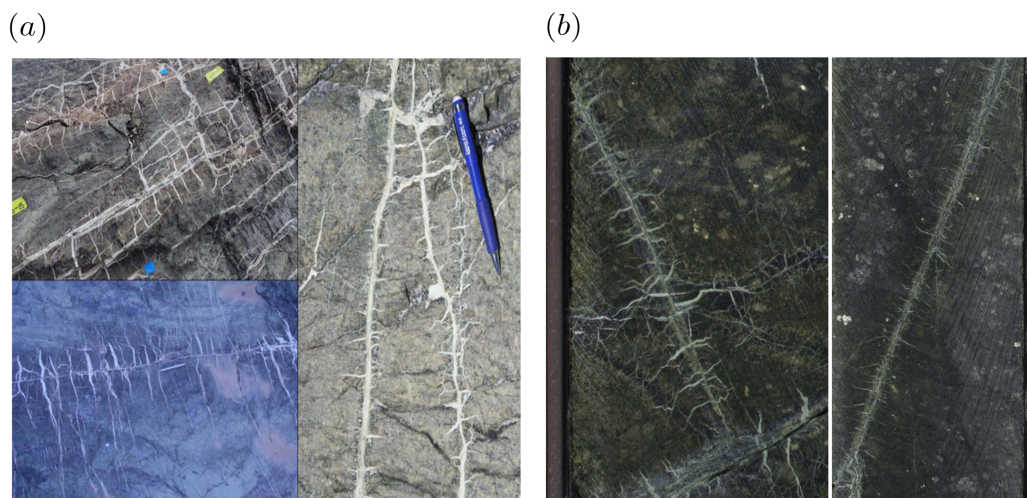


Figure 7. (a) Photos of peridotite outcrops in Oman: “Frankenstein” cracks (in this case filled with carbonate minerals) are characterized by central veins lined with a secondary set of orthogonally oriented cracks. It is often the case that these eventually terminate (i.e., the bottom right and left images), though in some cases (top left) a tertiary set of cracks forms off of this second set. (b) Photos of drill core sections showing “Frankenstein” cracks that are filled with serpentine.

5. Discussion and Conclusion

The model presented in this paper extends the authors’ previous work by incorporating failure into a model of small-strain poroelasticity that includes fluid flow and reaction. Throughout this study we focused specifically on olivine hydration, though the model could be easily modified to describe other reactions. For the failure component of the model we adopted a phase-field approach, which has the advantage of being a continuum method. Using parameters relevant to near-surface serpentinization, this new model demonstrates the positive feedback between reaction and failure that is central to the reaction-driven cracking hypothesis: Reaction-driven volume changes lead to the opening of Mode I cracks, in turn creating new porosity/reactive surface area and providing fast pathways for fluid transport from boundaries/external sources, which has the overall effect of increasing the extent of reaction. Crucially, this set of models also demonstrates that crack propagation provides a mechanism for fluid transport to regions that are almost impermeable initially.

The first of the failure models presented in section 4.2 demonstrates the positive feedback of reaction-driven cracking; however, the total amount of reaction in this model (a maximum of ~13% serpentinization given a starting porosity of ~4–5%) falls on the lower end of the spectrum of serpentinization/carbonation observed in natural systems. This is likely to be reflective of the fact that this model was run under fairly restricted conditions, that is, in the absence of external forcings such as an applied stress field or fluid pressure gradient. The importance of such factors is currently not well understood as the conditions necessary to achieve significant serpentinization/carbonation remain poorly constrained by observations and unexplored in modeling studies. In section 4.3 we showed that the presence of a background differential stress field can increase the maximum extent of reaction and for sufficiently large stresses (exceeding 0.5-MPa vertical tension for the presented model) can produce 100% conversion of olivine to serpentine in the cracks. Similarly, in section 4.4 we showed that a background fluid pressure gradient can increase the input of fluid into the system (via transport in cracks), which for pressure gradients on the order of hydrostatic values also results in 100% serpentinization in cracks. In section 4.5 the model was further explored by adding a nonadvective flux term representing the diffusion of water in cracks (driven by gradients in chemical potentials), which leads to a dramatic increase in the maximum extent and areal distribution of reaction, and the formation of multiple generations of cracks. The continued development of this feedback could eventually reproduce the orthogonal crack textures that are often seen in peridotite outcrops (see e.g., de Obeso and Kelemen, 2018; Iyer et al., 2008; Kelemen et al., 2011).

Although this model shows promise in its ability to simulate reaction-driven cracking over a range of different conditions, there remains room for improvement in the model formulation and opportunity to explore it further in future work. One issue with the current formulation is that, while linear poroelasticity may

be a good model for the early stages of serpentinization, it is arguably insufficient to describe the behavior after significant fracturing has taken place. More complex rheologies (e.g., large deformation elastoplasticity (Carter et al., 1979)) are probably more appropriate to describe the long-term behavior of these materials. Another neglected aspect of the model that would likely affect these results is the potential for damaged regions to regain some mechanical integrity due to precipitation of reaction products. This could lead to multiple cracking events, for example, “crack-seal” processes (Andreani et al., 2004; Hooker and Katz, 2015), in which cracks fill with reaction products, and then crack again. In the results that generate “Frankenstein” crack patterns (section 4.5 and Figure 6), the stress is eventually relaxed and the cracks cease to propagate further. It is, however, plausible that the continuation of the process demonstrated here could lead to the orthogonal networks that are observed in outcrops. Evidence of terminating veins suggests that crack propagation is—under certain conditions—limited, which may be due to a number of factors, for example, a diminished fluid supply or sufficient stress relaxation. The results in section 4.5 suggest that reactant supply (here controlled by diffusion of dissolved species) can control the areal extent of fracture networks. A thorough exploration of the conditions that lead to the possibility of multiple generations of orthogonal veins should be considered in future work. The integration of a consistent thermodynamic description of the reactions is another important direction for model development. Although thermodynamic feedbacks might not play a critical role in the first-order mechanical behavior for the simplified hydration reaction considered here, they could be important when modeling multiple dissolution/precipitation reactions involving mixed H₂O-CO₂ fluids, which will be important in models of geological carbon sequestration.

The stresses that are calculated in this model are purely poromechanical, resulting from local variations in volume changes that are due to reaction. An alternative form of stress that has been hypothesized to drive reaction-driven cracking in these systems is the so-called “crystallization pressure” or “force of crystallization.” The crystallization pressure is the local stress (in excess of the confining pressure) that is driven by crystal growth in pores, where the supply of ions is facilitated by a fluid nanofilm separating the growing crystal and the rock surface (see e.g., Correns, 1949; Scherer, 1999; Steiger, 2005). Kelemen and Hirth (2012) developed a model that estimates the crystallization pressure assuming complete conversion of chemical potential energy to changes in pressure, that is, that $P' = -\Delta_r G / \Delta V_s$ (where P' is the crystallization pressure, $\Delta_r G$ is the Gibbs Free Energy change for the reaction and ΔV_s is the difference in solid volume between reactants and products). Under this assumption they estimate crystallization pressures of ~300–500 MPa for hydration/carbonation reactions at temperatures of ~200–300 °C, comfortably exceeding the fracture strength of crustal rocks. Reaction-driven cracking observed during olivine carbonation experiments (Xing et al., 2018; Zhu et al., 2016) was not ascribed to crystallization pressure, but rather to tensile stresses (below the the confining pressure) that were generated by mismatches in volume changes across the sample. Similarly, the results presented in this paper demonstrate the possibility of reaction-driven cracking without appealing to the crystallization pressure hypothesis. Given the considerable uncertainty regarding the physics of these processes, however, it would be useful to explore and compare different failure mechanisms by extending the current formulation to calculate both poromechanical stresses and stresses associated with crystallization pressures. One approach would be to include a multiphase fluid that contains both water and dissolved solid components. An example of such an approach is the theoretical framework proposed by Choo and Sun (2018), which describes crystallization-induced deformation in porous media and assumes a constitutive form for the crystallization pressure based on the model in Kelemen and Hirth (2012).

To our knowledge, this is the first study that includes feedbacks between stress, reaction, fluid flow, and permeability in a model of reaction-driven cracking. It highlights that the inclusion of Darcian fluid flow—largely neglected in previous modeling efforts—is critical to constraining whether positive feedbacks (cracking) succeed in prevailing over negative ones (clogging). Without this, constraints on the conditions that lead to 100% serpentinization/carbonation will remain speculative. While this model does demonstrate the possibility of 100% serpentinization in cracks, a more complete understanding of its behavior (and limitations) still demands a thorough examination of the range of responses in a large parameter space. Moreover,

it remains uncertain how to produce near complete serpentinization of the whole rock (say, at least 60% or greater serpentinization), which is observed in places. Benchmarking the model against experiments is also a priority in future studies, so that comparisons with natural systems can be made with a higher degree of confidence.

Acknowledgments

We thank the Editor, two anonymous referees, and Richard Katz for constructive reviews that have improved this manuscript. An archived version of the code used in this study is publicly accessible at <https://zenodo.org/record/3541059> (DOI: 10.5281/zenodo.3541059). This work is supported by the National Science Foundation (Grants EAR-1520732 and EAR-1516300). Numerical simulations were run on computing resources from Columbia University's Shared Research Computing Facility project, which is supported by NIH Research Facility Improvement Grant 1G20RR030893-01 and associated funds from the New York State Empire State Development, Division of Science Technology and Innovation (NYSTAR) Contract C090171, both awarded 15 April 2010.

References

- Abramson, E., Brown, J., Slutsky, L., & Zaug, J. (1997). The elastic constants of san carlos olivine to 17 Gpa. *Journal of Geophysical Research*, 102(B6), 12,253–12,263.
- Alnæs, M. S., Blechta, J., Hake, J., Johansson, A., Kehlet, B., Logg, A., et al. (2015). The fenics project version 1.5. *Computational Mechanics*, 55(2), 383–405.
- Ambati, M., Gerasimov, T., & De Lorenzis, L. (2015). A review on phase-field models of brittle fracture and a new fast hybrid formulation. *Computational Mechanics*, 55(2), 383–405.
- Ambrosio, L., & Tortorelli, V. M. (1990). Approximation of functional depending on jumps by elliptic functional via t-convergence. *Communications on Pure and Applied Mathematics*, 43(8), 999–1036.
- Amor, H., Marigo, J.-J., & Maurini, C. (2009). Regularized formulation of the variational brittle fracture with unilateral contact: Numerical experiments. *Journal of the Mechanics and Physics of Solids*, 57(8), 1209–1229.
- Andreani, M., Baronnet, A., Boullier, A.-M., & Gratier, J.-P. (2004). A microstructural study of a “crack-seal” type serpentine vein using SEM and TEM techniques. *European Journal of Mineralogy*, 16(4), 585–595.
- Bahr, H.-A., Weiss, H.-J., Maschke, H., & Meissner, F. (1988). Multiple crack propagation in a strip caused by thermal shock. *Theoretical and Applied Fracture Mechanics*, 10(3), 219–226.
- Balay, S., Abhyankar, S., Adams, M., Brown, J., Brune, P., Buschelman, K., et al. (2019). Petsc users manual.
- Bear, J., & Cheng, A. H.-D. (2010). *Modeling groundwater flow and contaminant transport* (Vol. 23). Dordrecht, Netherlands: Springer Science & Business Media.
- Bercovici, D., Ricard, Y., & Schubert, G. (2001). A two-phase model for compaction and damage: 1. general theory. *Journal of Geophysical Research*, 106, 8887–8906. <https://doi.org/10.1029/2000JB900430>
- Bonnet, E., Bour, O., Odling, N. E., Davy, P., Main, I., Cowie, P., & Berkowitz, B. (2001). Scaling of fracture systems in geological media. *Reviews of Geophysics*, 39, 347–383. <https://doi.org/10.1029/1999RG000074>
- Borden, M. J., Hughes, T. J., Landis, C. M., Anvari, A., & Lee, I. J. (2016). A phase-field formulation for fracture in ductile materials: Finite deformation law derivation, plastic degradation, and stress triaxiality effects. *Computer Methods in Applied Mechanics and Engineering*, 312, 130–166.
- Borden, M. J., Hughes, T. J., Landis, C. M., & Verhoosel, C. V. (2014). A higher-order phase-field model for brittle fracture: Formulation and analysis within the isogeometric analysis framework. *Computer Methods in Applied Mechanics and Engineering*, 273, 100–118.
- Borden, M. J., Verhoosel, C. V., Scott, M. A., Hughes, T. J., & Landis, C. M. (2012). A phase-field description of dynamic brittle fracture. *Computer Methods in Applied Mechanics and Engineering*, 217, 77–95.
- Bourdin, B., Francfort, G. A., & Marigo, J.-J. (2000). Numerical experiments in revisited brittle fracture. *Journal of the Mechanics and Physics of Solids*, 48(4), 797–826.
- Bourdin, B., Marigo, J.-J., Maurini, C., & Sicsic, P. (2014). Morphogenesis and propagation of complex cracks induced by thermal shocks. *Physical Review Letters*, 112(1), 014301.
- Cai, M. (2010). Practical estimates of tensile strength and Hoek–Brown strength parameter m i of brittle rocks. *Rock Mechanics and Rock Engineering*, 43(2), 167–184.
- Carter, J., Booker, J., & Small, J. (1979). The analysis of finite elasto-plastic consolidation. *International Journal for Numerical and Analytical Methods in Geomechanics*, 3(2), 107–129.
- Chambolle, A. (2004). An approximation result for special functions with bounded deformation. *Journal de Mathématiques Pures et Appliquées*, 83(7), 929–954.
- Chavagnac, V., Ceuleneer, G., Monnin, C., Lansac, B., Hoareau, G., & Boulart, C. (2013). Mineralogical assemblages forming at hyperalkaline warm springs hosted on ultramafic rocks: A case study of oman and ligurian ophiolites. *Geochemistry, Geophysics, Geosystems*, 14, 2474–2495. <https://doi.org/10.1029/ggge.20146>
- Chavagnac, V., Monnin, C., Ceuleneer, G., Boulart, C., & Hoareau, G. (2013). Characterization of hyperalkaline fluids produced by low-temperature serpentinization of mantle peridotites in the Oman and Ligurian ophiolites. *Geochemistry, Geophysics, Geosystems*, 14, 2496–2522. <https://doi.org/10.1029/ggge.20147>
- Cheng, A. H.-D. (2016). *Poroelasticity* (Vol. 27). Switzerland: Springer International Publishing.
- Choo, J., & Sun, W. (2018). Cracking and damage from crystallization in pores: Coupled chemo-hydro-mechanics and phase-field modeling. *Computer Methods in Applied Mechanics and Engineering*, 335, 347–379.
- Correns, C. W. (1949). Growth and dissolution of crystals under linear pressure. *Discussions of the Faraday Society*, 5, 267–271.
- Craft, K. L., & Lowell, R. P. (2009). A boundary layer model for submarine hydrothermal heat flows at on-axis and near-axis regions. *Geochemistry, Geophysics, Geosystems*, 10, Q12012. <https://doi.org/10.1029/2009GC002707>
- De Groot, S. R., & Mazur, P. (2013). *Non-equilibrium thermodynamics*. North Chelmsford: Courier Corporation.
- de Obeso, J. C., & Kelemen, P. B. (2018). Fluid rock interactions on residual mantle peridotites overlain by shallow oceanic limestones: Insights from Wadi Fins, Sultanate of Oman. *Chemical Geology*, 498, 139–149.
- Dewandel, B., Lachassagne, P., Boudier, F., Al-Hattali, S., Ladouche, B., Pinault, J.-L., & Al-Suleimani, Z. (2005). A conceptual hydrogeological model of ophiolite hard-rock aquifers in Oman based on a multiscale and a multidisciplinary approach. *Hydrogeology Journal*, 13(5-6), 708–726.
- Escarlin, J., Hirth, G., & Evans, B. (2001). Strength of slightly serpentinized peridotites: Implications for the tectonics of oceanic lithosphere. *Geology*, 29(11), 1023–1026.
- Evans, O., Spiegelman, M., & Kelemen, P. B. (2018). A poroelastic model of serpentinization: Exploring the interplay between rheology, surface energy, reaction, and fluid flow. *Journal of Geophysical Research: Solid Earth*, 123, 8653–8675.
- Farrell, P., & Maurini, C. (2017). Linear and nonlinear solvers for variational phase-field models of brittle fracture. *International Journal for Numerical Methods in Engineering*, 109(5), 648–667.
- Francfort, G. A., & Marigo, J.-J. (1998). Revisiting brittle fracture as an energy minimization problem. *Journal of the Mechanics and Physics of Solids*, 46(8), 1319–1342.

- Freddi, F., & Royer-Carfagni, G. (2010). Regularized variational theories of fracture: A unified approach. *Journal of the Mechanics and Physics of Solids*, 58(8), 1154–1174.
- Goehring, L., Mahadevan, L., & Morris, S. W. (2009). Nonequilibrium scale selection mechanism for columnar jointing. *Proceedings of the National Academy of Sciences*, 106(2), 387–392.
- Griffith, A. A., & Eng, M. (1921). Vi. The phenomena of rupture and flow in solids. *Philosophical Transactions of the Royal Society A*, 221(582-593), 163–198.
- Gueguen, Y., & Dienes, J. (1989). Transport properties of rocks from statistics and percolation. *Mathematical Geology*, 21(1), 1–13.
- Hadley, K. (1976). Comparison of calculated and observed crack densities and seismic velocities in westerly granite. *Journal of Geophysical Research*, 81(20), 3484–3494.
- Hirauchi, K.-I., Fukushima, K., Kido, M., Muto, J., & Okamoto, A. (2016). Reaction-induced rheological weakening enables oceanic plate subduction. *Nature Communications*, 7, 12550.
- Hooker, J. N., & Katz, R. F. (2015). Vein spacing in extending, layered rock: The effect of synkinematic cementation. *American Journal of Science*, 315(6), 557–588.
- Iyer, K., Jamtveit, B., Mathiesen, J., Malthe-Sørensen, A., & Feder, J. (2008). Reaction-assisted hierarchical fracturing during serpentinization. *Earth and Planetary Science Letters*, 267(3-4), 503–516.
- Jamtveit, B., Malthe-Sørensen, A., & Kostenko, O. (2008). Reaction enhanced permeability during retrogressive metamorphism. *Earth and Planetary Science Letters*, 267(3-4), 620–627.
- Jiang, C., Wu, X., Li, J., Song, F., Shao, Y., Xu, X., & Yan, P. (2012). A study of the mechanism of formation and numerical simulations of crack patterns in ceramics subjected to thermal shock. *Acta Materialia*, 60(11), 4540–4550.
- Katz, R. F., Spiegelman, M., & Holtzman, B. (2006). The dynamics of melt and shear localization in partially molten aggregates. *Nature*, 442(7103), 676.
- Kelemen, P. B., & Hirth, G. (2012). Reaction-driven cracking during retrograde metamorphism: Olivine hydration and carbonation. *Earth and Planetary Science Letters*, 345, 81–89.
- Kelemen, P. B., & Manning, C. E. (2015). Reevaluating carbon fluxes in subduction zones, what goes down, mostly comes up. *Proceedings of the National Academy of Sciences*, 112(30), E3997–E4006.
- Kelemen, P. B., & Matter, J. (2008). In situ carbonation of peridotite for CO₂ storage. *Proceedings of the National Academy of Sciences*, 105(45), 17,295–17,300.
- Kelemen, P. B., Matter, J., Streit, E. E., Rudge, J. F., Curry, W. B., & Blusztajn, J. (2011). Rates and mechanisms of mineral carbonation in peridotite: Natural processes and recipes for enhanced, in situ CO₂ capture and storage. *Annual Review of Earth and Planetary Sciences*, 39, 545–576.
- Kelley, K. A., Plank, T., Grove, T. L., Stolper, E. M., Newman, S., & Hauri, E. (2006). Mantle melting as a function of water content beneath back-arc basins. *Journal of Geophysical Research*, 111(B9), B09208. <https://doi.org/10.1029/2005JB003732>
- Lackner, K. S., Wendt, C. H., Butt, D. P., Joyce, E. L. Jr., & Sharp, D. H. (1995). Carbon dioxide disposal in carbonate minerals. *Energy*, 20(11), 1153–1170.
- Lamadrid, H. M., Rimstidt, J. D., Schwarzenbach, E. M., Klein, F., Ulrich, S., Dolocan, A., & Bodnar, R. J. (2017). Effect of water activity on rates of serpentinization of olivine. *Nature Communications*, 8, 16107.
- Lambart, S., Savage, H., Robinson, B., & Kelemen, P. (2018). Experimental investigation of the pressure of crystallization of CA (OH)₂: Implications for the reactive cracking process. *Geochemistry, Geophysics, Geosystems*, 19(9), 3448–3458. <https://doi.org/10.1029/2018GC007609>
- Lee, S., Mikelić, A., Wheeler, M. F., & Wick, T. (2016). Phase-field modeling of proppant-filled fractures in a poroelastic medium. *Computer Methods in Applied Mechanics and Engineering*, 312, 509–541.
- Macdonald, A., & Fyfe, W. (1985). Rate of serpentinization in seafloor environments. *Tectonophysics*, 116(1-2), 123–135.
- Malthe-Sørensen, A., Jamtveit, B., & Meakin, P. (2006). Fracture patterns generated by diffusion controlled volume changing reactions. *Physical Review Letters*, 96(24), 245501.
- Malvoisin, B., Brantut, N., & Kaczmarek, M.-A. (2017). Control of serpentinisation rate by reaction-induced cracking. *Earth and Planetary Science Letters*, 476, 143–152.
- Manning, C., & Ingebretsen, S. (1999). Permeability of the continental crust: Implications of geothermal data and metamorphic systems. *Reviews of Geophysics*, 37(1), 127–150.
- Martin, W., Baross, J., Kelley, D., & Russell, M. J. (2008). Hydrothermal vents and the origin of life. *Nature Reviews Microbiology*, 6(11), 805–814.
- McCollom, T. M., Klein, F., Robbins, M., Moskowitz, B., Berqué, T. S., Jóns, N., et al. (2016). Temperature trends for reaction rates, hydrogen generation, and partitioning of iron during experimental serpentinization of olivine. *Geochimica et Cosmochimica Acta*, 181, 175–200.
- McKenzie, D. (1984). The generation and compaction of partially molten rock. *Journal of Petrology*, 25(3), 713–765.
- Mervine, E. M., Humphris, S. E., Sims, K. W., Kelemen, P. B., & Jenkins, W. J. (2014). Carbonation rates of peridotite in the Samail Ophiolite, Sultanate of Oman, constrained through ¹⁴C dating and stable isotopes. *Geochimica et Cosmochimica Acta*, 126, 371–397.
- Miehe, C., Hofacker, M., & Welschinger, F. (2010). A phase field model for rate-independent crack propagation: Robust algorithmic implementation based on operator splits. *Computer Methods in Applied Mechanics and Engineering*, 199(45-48), 2765–2778.
- Miehe, C., & Mauthe, S. (2016). Phase field modeling of fracture in multi-physics problems. Part III. Crack driving forces in hydro-poro-elasticity and hydraulic fracturing of fluid-saturated porous media. *Computer Methods in Applied Mechanics and Engineering*, 304, 619–655.
- Miehe, C., Welschinger, F., & Hofacker, M. (2010). Thermodynamically consistent phase-field models of fracture: Variational principles and multi-field fe implementations. *International Journal for Numerical Methods in Engineering*, 83(10), 1273–1311.
- Mikelic, A., Wheeler, M. F., & Wick, T. (2015). A phase-field method for propagating fluid-filled fractures coupled to a surrounding porous medium. *Multiscale Modeling and Simulation*, 13(1), 367–398.
- O'Hanley, D. S. (1992). Solution to the volume problem in serpentinization. *Geology*, 20(8), 705–708.
- Peacock, S. M. (2001). Are the lower planes of double seismic zones caused by serpentine dehydration in subducting oceanic mantle? *Geology*, 29(4), 299–302.
- Plümper, O., Botan, A., Los, C., Liu, Y., Malthe-Sørensen, A., & Jamtveit, B. (2017). Fluid-driven metamorphism of the continental crust governed by nanoscale fluid flow. *Nature Geoscience*, 10(9), 685–690.
- Ranero, C. R., Morgan, J. P., McIntosh, K., & Reichert, C. (2003). Bending-related faulting and mantle serpentinization at the middle america trench. *Nature*, 425(6956), 367.
- Roland, E., Behn, M. D., & Hirth, G. (2010). Thermal-mechanical behavior of oceanic transform faults: Implications for the spatial distribution of seismicity. *Geochemistry, Geophysics, Geosystems*, 11, Q07001. <https://doi.org/10.1029/2010GC003034>

- Rouméjon, S., & Cannat, M. (2014). Serpentinization of mantle-derived peridotites at mid-ocean ridges: Mesh texture development in the context of tectonic exhumation. *Geochemistry, Geophysics, Geosystems*, 15, 2354–2379. <https://doi.org/10.1002/2013GC005148>
- Røyne, A., Jamtveit, B., Mathiesen, J., & Malthe-Sørensen, A. (2008). Controls on rock weathering rates by reaction-induced hierarchical fracturing. *Earth and Planetary Science Letters*, 275(3–4), 364–369.
- Rudge, J. F., Bercovici, D., & Spiegelman, M. (2011). Disequilibrium melting of a two phase multicomponent mantle. *Geophysical Journal International*, 184(2), 699–718.
- Rudge, J. F., Kelemen, P. B., & Spiegelman, M. (2010). A simple model of reaction-induced cracking applied to serpentinization and carbonation of peridotite. *Earth and Planetary Science Letters*, 291(1–4), 215–227.
- Santillán, D., Juanes, R., & Cueto-Felgueroso, L. (2017). Phase field model of fluid-driven fracture in elastic media: Immersed-fracture formulation and validation with analytical solutions. *Journal of Geophysical Research: Solid Earth*, 122, 2565–2589. <https://doi.org/10.1002/2016JB013572>
- Santillán, D., Juanes, R., & Cueto-Felgueroso, L. (2018). Phase field model of hydraulic fracturing in poroelastic media: Fracture propagation, arrest, and branching under fluid injection and extraction. *Journal of Geophysical Research: Solid Earth*, 123, 2127–2155. <https://doi.org/10.1002/2017JB014740>
- Scherer, G. W. (1999). Crystallization in pores. *Cement and Concrete Research*, 29(8), 1347–1358.
- Seifritz, W. (1990). CO₂ disposal by means of silicates. *Nature*, 345(6275), 486–486.
- Sicsic, P., Marigo, J.-J., & Maurini, C. (2014). Initiation of a periodic array of cracks in the thermal shock problem: A gradient damage modeling. *Journal of the Mechanics and Physics of Solids*, 63, 256–284.
- Skarbek, R. M., Savage, H. M., Kelemen, P. B., & Yancopoulos, D. (2018). Competition between crystallization-induced expansion and creep compaction during gypsum formation, and implications for serpentinization. *Journal of Geophysical Research: Solid Earth*, 123, 5372–5393. <https://doi.org/10.1029/2017JB015369>
- Sleep, N., Meibom, A., Fridriksson, T., Coleman, R., & Bird, D. (2004). H₂-rich fluids from serpentinization: geochemical and biotic implications. *Proceedings of the National Academy of Sciences*, 101(35), 12,818–12,823.
- Spiegelman, M., Kelemen, P. B., & Aharonov, E. (2001). Causes and consequences of flow organization during melt transport: The reaction infiltration instability in compatiblie media. *Journal of Geophysical Research*, 106, 2061–2077. <https://doi.org/10.1029/2000JB900240>
- Steiger, M. (2005). Crystal growth in porous materials—I: The crystallization pressure of large crystals. *Journal of Crystal Growth*, 282(3–4), 455–469.
- Timoshenko, S., & Goodier, J. (1970). *Theory of elasticity*. New York: McGraw-Hill.
- Ulven, O., Jamtveit, B., & Malthe-Sørensen, A. (2014). Reaction-driven fracturing of porous rock. *Journal of Geophysical Research: Solid Earth*, 119, 7473–7486.
- Ulven, O., Storheim, H., Austrheim, H., & Malthe-Sørensen, A. (2014). Fracture initiation during volume increasing reactions in rocks and applications for CO₂ sequestration. *Earth and Planetary Science Letters*, 389, 132–142. <https://doi.org/10.1002/2014JB011102>
- Van Avendonk, H. J., Holbrook, W. S., Lizarralde, D., & Denyer, P. (2011). Structure and serpentinization of the subducting Cocos Plate offshore Nicaragua and Costa Rica. *Geochemistry, Geophysics, Geosystems*, 12, Q06009. <https://doi.org/10.1029/2011GC003592>
- Verhoosel, C. V., & de Borst, R. (2013). A phase-field model for cohesive fracture. *International Journal for Numerical Methods in Engineering*, 96(1), 43–62.
- Vermilye, J. M., & Scholz, C. H. (1995). Relation between vein length and aperture. *Journal of Structural Geology*, 17(3), 423–434.
- Wilson, C. R., Spiegelman, M., & van Keeken, P. E. (2017). Terraferma: The transparent finite element rapid model assembler for multiphysics problems in Earth sciences. *Geochemistry, Geophysics, Geosystems*, 18, 769–810. <https://doi.org/10.1002/2016GC006702>
- Wolterbeek, T. K., van Noort, R., & Spiers, C. J. (2018). Reaction-driven casing expansion: Potential for wellbore leakage mitigation. *Acta Geotechnica*, 13(2), 341–366.
- Wu, Y.-S., Ye, M., & Sudicky, E. (2010). Fracture-flow-enhanced matrix diffusion in solute transport through fractured porous media. *Transport in Porous Media*, 81(1), 21.
- Wu, Y.-S., Zhang, K., & Liu, H.-H. (2006). Estimating large-scale fracture permeability of unsaturated rock using barometric pressure data. *Vadose Zone Journal*, 5(4), 1129–1142.
- Xing, T., Zhu, W., Fusseis, F., & Lisabeth, H. (2018). Generating porosity during olivine carbonation via dissolution channels and expansion cracks. *Solid Earth (online)*, 9(4), 879–896.
- Zheng, X., Cordonnier, B., Zhu, W., Renard, F., & Jamtveit, B. (2018). Effects of confinement on reaction-induced fracturing during hydration of periclase. *Geochemistry, Geophysics, Geosystems*, 19, 2661–2672. <https://doi.org/10.1029/2017GC007322>
- Zhu, W., Fusseis, F., Lisabeth, H., Xing, T., Xiao, X., De Andrade, V., & Karato, S.-I. (2016). Experimental evidence of reaction-induced fracturing during olivine carbonation. *Geophysical Research Letters*, 43, 9535–9543. <https://doi.org/10.1002/2016GL070834>